





## RESEARCH ARTICLE

10.1029/2021GC009879

## From Subduction to LLSVP: The Core-Mantle Boundary Heterogeneities Across North Atlantic

 An Fan<sup>1,2</sup>, Xinlei Sun<sup>1,3</sup> , Zhou Zhang<sup>1,2</sup> , Peng Zhang<sup>1,2</sup>, and Jianye Zong<sup>3</sup>

<sup>1</sup>State Key Laboratory of Isotope Geochemistry, Guangzhou Institute of Geochemistry, Chinese Academy of Sciences, Guangzhou, China, <sup>2</sup>University of Chinese Academy of Sciences, Beijing, China, <sup>3</sup>International Center for Planetary Science, College of Geosciences, Chengdu University of Technology, Chengdu, China

**Key Points:**

- A structural transition from D" layer to a high-velocity layer and Ultra-low Velocity Zones is found from mid-Atlantic to the northwest boundary of the African Large Low Shear Velocity Zones (LLSVP)
- These core mantle boundary heterogeneities are very likely from interactions of paleo-subducted Farallon slab with ambient mantle and LLSVP material
- The low velocity layer at the top of D" discontinuity may be caused by compositional change from subducted slab

**Supporting Information:**

Supporting Information may be found in the online version of this article.

**Correspondence to:**

X. Sun,  
xsun@cdu.edu.cn

**Citation:**

Fan, A., Sun, X., Zhang, Z., Zhang, P., & Zong, J. (2022). From subduction to LLSVP: The core-mantle boundary heterogeneities across north Atlantic. *Geochemistry, Geophysics, Geosystems*, 23, e2021GC009879. <https://doi.org/10.1029/2021GC009879>

Received 3 MAY 2021  
Accepted 10 OCT 2021

© 2021. The Authors.

This is an open access article under the terms of the [Creative Commons Attribution-NonCommercial-NoDerivs License](https://creativecommons.org/licenses/by-nc-nd/4.0/), which permits use and distribution in any medium, provided the original work is properly cited, the use is non-commercial and no modifications or adaptations are made.

**Abstract** The distribution of Ultra-low Velocity Zones (ULVZs) is generally associated with the Large Low Shear Velocity Zones (LLSVPs). However, subducted slabs may be important for the characteristics of the ULVZs as well. Here we use ScS precursor (SdS) and postcursor (ScscS) phases, as well as Scd phases recorded by USArray to investigate the lowermost mantle structure across the north Atlantic, which spans the African LLSVP and the subducted Farallon slab. Our results show a ULVZ located near the edge of the African LLSVP, with thicknesses ranging from 11–16 km and S wave velocity reductions of 12%–24%. At the same time, a thin high-velocity layer (HVL) with thicknesses of 20–30 km, Vs increases of 3%–4%, is also detected outside the LLSVP in the northwest region. Further west there is a clear D" layer at 250 km above the core mantle boundary (CMB), overlaid by a low velocity layer with Vs reduction of 3%. This transition profile from D" to HVL to ULVZ provides an excellent opportunity for us to understand the heterogeneities near the CMB region. We propose that interactions between the subducted Farallon slab with ambient mantle and LLSVP material, together with thermal effects, may result in this transition between different seismic structures along the CMB.

### 1. Introduction

In the past few decades, seismological studies have demonstrated complex structures near the core mantle boundary (CMB). Among them, ultra-low velocity zones (ULVZs) and their relationship to the Large Low Shear Low Velocity Provinces (LLSVPs), subducted slabs and the D" layer, attract great interest.

LLSVPs (Large Low Shear Velocity Provinces) are two broad areas in the lowermost mantle below Africa and the Pacific, where S wave velocity is lower than the average. The height of LLSVP is about hundreds of kilometers and the width is of thousands of kms (He & Wen, 2009, 2012; Ni & Helmberger, 2003; Ni et al., 2002). Understanding the composition of LLSVP, as well as the related structures in and around it provides first order implications to our understanding of the evolution in the lower mantle.

ULVZs in general have lateral scales from several tens to about one thousand kms, and thicknesses in several to several tens of kilometers (e.g., Cottaar & Romanowicz, 2012; He & Wen, 2009; Ma et al., 2019; Thorne & Garnero, 2004), Vp and Vs reduction up to 25% and 50% (e.g., Brown et al., 2015; Rondenay & Fischer, 2003), and density increase is up to 10%, respectively (e.g., Rost et al., 2006). Several hypotheses have been proposed to explain observed ULVZs, referring their formation to partial melting (Berryman, 2000; Williams & Garnero, 1996), remnants of a basal magma ocean (Labrosse et al., 2007; Nomura et al., 2011), chemical reactions between mantle materials with the core (Buffett et al., 2000), iron enriched mantle materials (e.g., Mao et al., 2006; Wicks et al., 2010), or involvement of chemical compositions from subducted slabs (Christensen & Hofmann, 1994; Hu et al., 2016; Liu et al., 2016).

On the other hand, the D" region, which is characterized by a discontinuity at ~100–300 km above the CMB and represents compositional and thermal changes in the lowermost mantle, is generally attributed to slab debris (e.g., Masters et al., 2000; Sun et al., 2006). D" has been detected mostly around the circum-Pacific (e.g., Montelli et al., 2004; Ritsema et al., 1998; Simmons et al., 2011). Previous studies show that D" displays complex characteristics in terms of its depth, velocity gradient and composition (e.g., Sun et al., 2013, 2018; Wicks et al., 2010; Wysession et al., 1998), which are important for unraveling the thermal and compositional dynamics of the CMB.

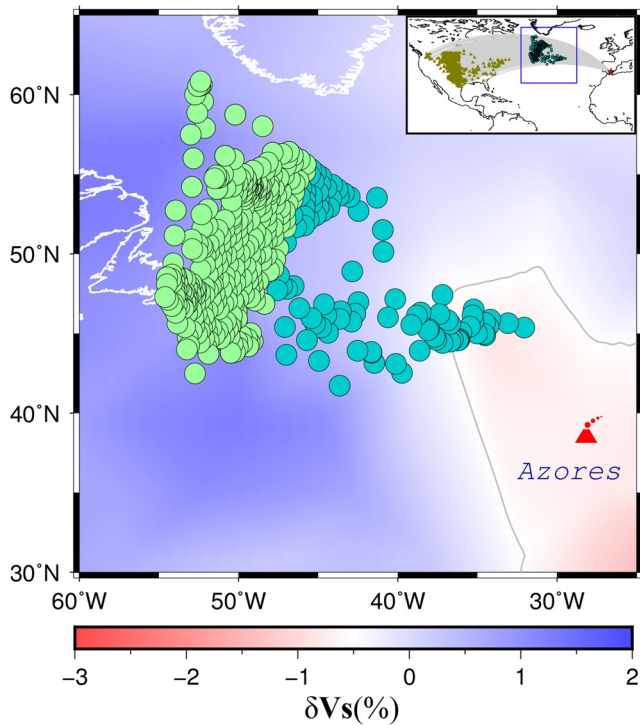


**Figure 1.** ScS data used in this study. Red stars, yellow triangles and the gray lines in the upper right corner represent earthquakes, stations and ScS raypaths, respectively. Whereas red volcano symbol represents a hotspot and green circles represent ScS CMB bounce points. Light green and dark green circles are the data having S<sub>cd</sub> signal and S<sub>u</sub> energy, respectively. Background is the S wave tomography of GyPSuM (Simmons et al., 2010), and the thick gray line is the contour line of  $-0.5\%$  velocity reduction, which roughly represent the African Large Low Shear Velocity Zones boundary.

Seismic studies show that the distribution of ULVZs is generally associated with the LLSVP (see review by Yu & Garnero, 2018). Most detected ULVZs seem to be clustered inside and at the boundary of the LLSVPs (e.g., Avants et al., 2006; Cottaar & Romanowicz, 2012; Helmberger et al., 2000; Thorne et al., 2013), while some ULVZs have been observed near the subducted slabs (Yao & Wen, 2014). On the other hand, both D'' and ULVZ could coexist near the LLSVP boundary (e.g., Sun et al., 2019; Tao et al., 2020). For example, studies show that around the north boundary of the Pacific LLSVP, slabs (related to D'' structures) and ULVZs are observed in the same region (He & Wen, 2009, 2012; Sun et al., 2019). Isolated ULVZs are also observed at the eastern boundary of the Pacific LLSVP, which may also be related to active subductions nearby (e.g., Deng et al., 2017; Ma et al., 2019). All these results suggest complex interactions of the LLSVP with the surrounding mantle.

Although ULVZs associated with the Pacific Ocean have been extensively investigated (e.g., Cottaar & Romanowicz, 2012; Courtier et al., 2007; Ma et al., 2019; Thorne et al., 2013), due to the limitations of data, only a few ULVZs have been found around the African LLSVP (e.g., Ma & Sun, 2017; Rost & Garnero, 2006; Simmons & Grand, 2002; Vanacore et al., 2016). Moreover, interactions of the African LLSVP and structures in the lower mantle are seldom investigated. The Pacific and African LLSVPs are different in terms of their heights (Pacific LLSVP, few hundred kms; African LLSVP, few hundreds of kms to over a thousand kms, e.g., He & Wen, 2012; Ni & Helmberger, 2003; Sun & Miller, 2013), their velocities (e.g., He & Wen, 2009; Ni et al., 2002), compositions and their boundaries (e.g., He & Wen, 2012; Wang & Wen, 2007). Moreover, active subducting slabs exist around the Pacific LLSVP yet it is not the case for the African LLSVP. Considering the similarities and differences of the Pacific and African LLSVPs, it is necessary to probe more structures in and around the African LLSVP and compare them with those in the Pacific LLSVP, so as to better understand lower mantle dynamics, such as whether these differences can affect ULVZ and/or D'' locations.

In this study, using ScS data recorded by USArray, we investigated different CMB structures in a long profile in north Atlantic, across the northwest boundary of the African LLSVP and the east end of Farallon slab (Figure 1). The changes of the ULVZ to thin high-velocity layer to D'' from east to west direction suggest that in regions without active subduction, materials from different structures may interact and mix with ambient mantle and finally result in a smooth transition.

## 2. Data

Our study region is near the northwest boundary of African LLSVP (Figure 1). Considering data availability and our need for CMB structure detection, we choose ScS waveforms to investigate the CMB structures. We systematically search earthquakes from 2000 to 2020 in Europe. In the search process, we require the earthquakes to have focal depth deeper than 100 km, magnitude greater than 5.5, and have simple source time functions to ensure good signal-to-noise ratio (SNR). We also require the epicentral distances of the data to be between 30°–80°, thus clear ScS phases can be identified. Finally, we obtain the data set with one event in Strait of Gibraltar (Table 1), which is recorded in USArray with excellent ScS waveforms in an epicentral distance range 45°–80° (Figure 1).

According to the characteristics of the signal, our data can be divided into two groups (Figure 1). One group is in distance range of 45°–70° (dark green points in Figure 1), in which we find ScS precursor and postcursor signals to constrain small-scale structures such as ULVZ near the CMB. The other group is in distances greater than 70° (light green points in Figure 1), in which we find clear S<sub>cd</sub> phases and use them to detect D'' structures (details

**Table 1**  
An Event for This Study

Date	Time	Lat	Lon	Depth	Mag.
2010-04-11	22:24:05	37.0075	-3.4764	619.6	6.3

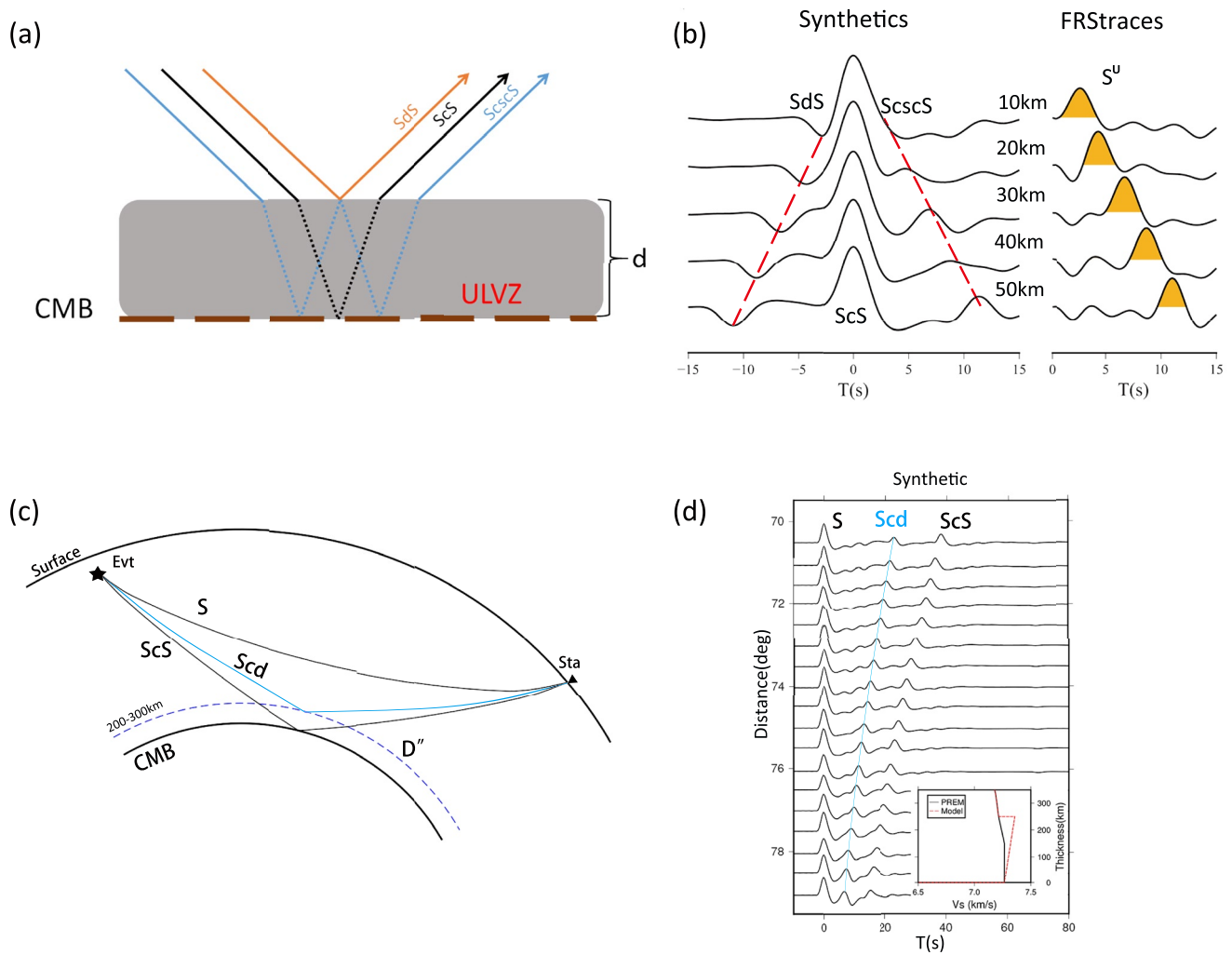


**Figure 2.** Illustration of seismic ray paths and waveforms related to Ultra-low Velocity Zones (ULVZ) and D'' discontinuity layer structures. (a) Raypath of ScS, ScS precursors (SdS) and ScS postcursors (ScscS) for a model with ULVZ. (b) (Left) Synthetic seismograms calculated from ULVZ models with 30% S wave velocity reduction and different thicknesses. The seismograms are aligned with ScS and the ULVZ thickness is labeled on the left side of each seismogram. (Right) The traces are obtained by using FRS technique. S<sup>U</sup> represents ULVZ signal. (c) Ray-paths of S, Scd and ScS for a D'' discontinuity model. (d) Example synthetic waveforms from a typical D'' discontinuity model at the right bottom, S phases are aligned at 0 time. The blue line represents arrive time of Scd phase, and the third phase is ScS phase.

are in Section 4). It is to note here that all the data are processed the same way (both ScS precursor and postcursors, as well as Scd signals are investigated), but different signals are found in different distance ranges.

ScS precursor (SdS) and postcursor (ScscS) are reflections of S wave at the two boundaries of ULVZ (Figures 2a and 2b), thus their positions and amplitudes are reflections of the characteristics of the ULVZ structure. On the other hand, Scd waveforms are reflections of S wave from above the D'' discontinuity, and their energy as well as emerging distances are all used to constrain the D'' characteristics (Figures 2c and 2d).

In the following sections, we investigate separately these two sets of data, and show different structures of a near east-west profile near the CMB.

### 3. ULVZ Near the Boundary of the African LLSVP

#### 3.1. Signal Extraction

We follow Zhao et al. (2017) apply flip-reverse-stack (FRS) method to enhance the ULVZ signals (ScS precursor and postcursor, if there is any). In this method, we cut the peak/trough of ScS phase, flip and reverse half of the

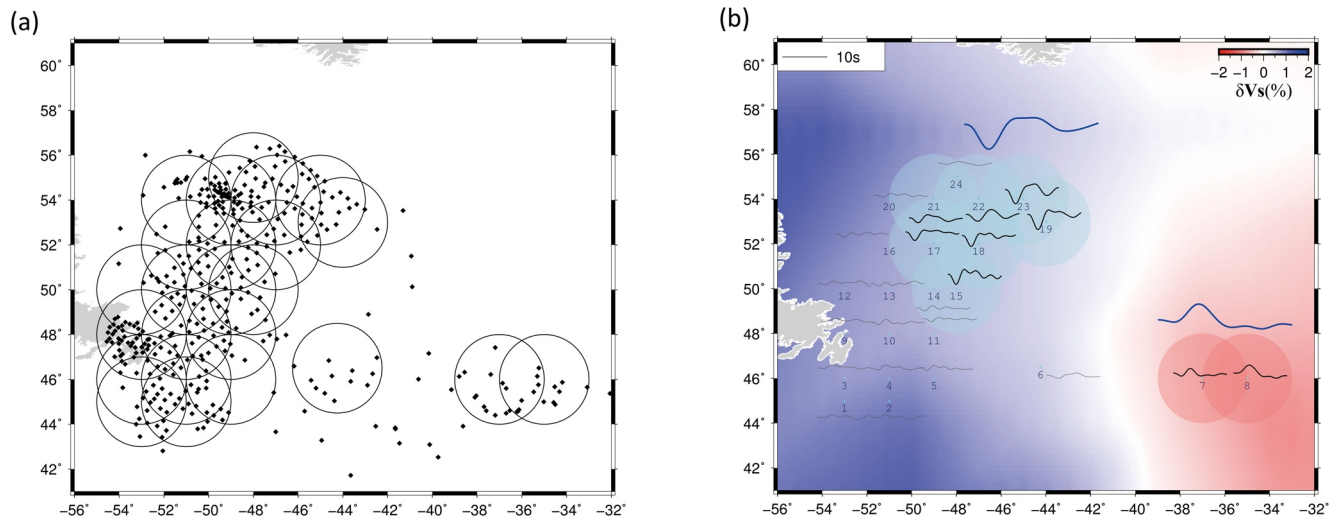


**Figure 3.** Summary map of bin distribution and final stack traces of ScS precursors and postcursors. (a) Original bin locations in the northwest boundary of African Large Low Shear Velocity Zones. Each bin has a 2° radius. Black dots are ScS bouncing points from all data set. (b) Traces with clear S<sup>U</sup> phase are shown in black, while traces with weak/no S<sup>U</sup> phase are shown in gray. The thick blue traces are the final FRS traces from different bins (light blue and light red circles), one displays positive and the other displays negative peaks. Background is S velocity tomography model from GyPSuM (Simmons et al., 2010).

waveform and stack it with the remaining half. In this way, the main ScS phase is canceled out, yet the precursor and postcursor of ScS are enhanced (Figure 2b).

In our data processing, we first remove the instrument response of all recordings, and then rotate them into great circle path to obtain radial and transverse components (for simplicity, we only use S<sub>H</sub> waves); bandpass filtering (corner frequency ranges from 0.015 to 0.3 Hz) is also applied. We cut these S<sub>H</sub> waveforms in 40s time windows, which center on both S and ScS phases for further processing.

We use stacked S waves as source time function and deconvolve it with ScS to remove the earthquake source effect. It is noted that the length (or the frequency content) of the stacked S and ScS phases are not always the same, so we compress or stretch S phase before deconvolution, which can minimize the effects of different paths (details can also be found in Zhao et al., 2017).

The deconvolution method applied is a wavelet deconvolution (Berkhout, 1977). Basically, in the time domain, it generates a wavelet inverse filter and calculate the least-square differences between the observed waveforms and the desired delta-like spike function of normalized amplitude. In this study, we deconvolve a delta function by the S phase to get an inverse filter, and then apply the filter to the ScS phase to obtain the deconvolution result. The algorithm used to obtain the inverse filter from the delta function and the S phase is the Wiener-Levinson algorithm (Levinson, 1946). To validate this deconvolution method, we test synthesized waveform with an epicenter distance from 45° to 70°, and the results are shown in Figure S1 in Supporting Information S1.

In the next step, we divide the CMB region into different bins according to ScS bounce points: We first divide the bins according to latitude and longitude, with each bins having a two-degree radius (about 130 km at the CMB); we then check the number of data observations in these bins and delete those with less than 10. Finally the bin locations are adjusted to accommodate as much data as possible (Figure 3a).

In each bin, we deconvolve the stacked S wave from each ScS waveform, as described earlier. Quality-control is performed on the source-deconvolved waveforms. We first choose those with a signal noise ratio (SNR) higher than 5, and then check them again by eye, discarding recordings without clear S and ScS phases. Then we use an iterative linear weighted stacking approach (Rawlinson & Kennett, 2004) to stack FRS traces. Twenty four stacked FRS traces are obtained after the stack (as shown in Figure 3b). We then stack the traces with similar shapes again (e.g., traces 7 and 8 in Figure 3b). Finally, we have two FRS traces, one has a positive peak and the other has negative peak (blue traces in Figure 3b).

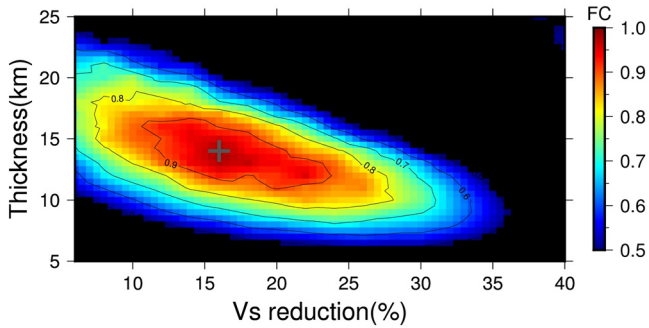


**Figure 4.** Fit coefficient (FC) map. The horizontal and vertical axis represents Vs reduction and thickness of Ultra-low Velocity Zones, respectively. Colors represent the value of FC. Black cross is the best fit model, and good models are defined as those with FC > 0.9.

### 3.2. Structure Modeling

Our waveform modeling shows that the stacked positive and negative waveforms are generated by negative (ULVZ) and positive velocity changes (high-velocity layer, HVL) above the CMB, respectively. We apply a grid search method to find the proper structures for each type of wave. First, we generate a database including a set of different ULVZ or HVL models. The thicknesses of ULVZ models change from 5 to 40 km, S velocities change from  $-40\%$  to  $0\%$  km/s, and density change from  $0\%$  to  $10\%$ . Each model has thickness increment of 1 km, density increment of  $2\%$  and velocity decrease of  $2\%$ , respectively. For the HVL model, the thicknesses are from 5 to 40 km, S velocities change from  $0\%$  to  $4\%$  km/s, and density change from  $0\%$  to  $10\%$ . The changes of the model thickness, density and velocity are 5 km,  $2\%$  and  $1\%$ , respectively.

3480 1-D ULVZ and 140 HVL models are generated. For each model, we synthesize S waveforms via direct solution method (Cummins et al., 1997; Kawai et al., 2006), process them according to methods described earlier, and get the corresponding FRS traces. We use these synthetic FRS traces as a database, and search within it, to find the best fitting model for our two regional data stacks. We define the fit coefficient (FC) using following equations, which is calculated considering the waveform cross correlation coefficient (CCC) as well as the shapes (amplitude and width) of the waveforms:

$$FC = CCC * M_A * M_B \quad (1)$$

$$M_A = \sum (1 - |A_{syn} - A_{data}| / A_{syn}) \quad (2)$$

$$M_B = [1 - (|W_{syn} - W_{data}| / W_{syn})] * [1 - (|P_{syn} - P_{data}| / P_{syn})] \quad (3)$$

where  $M_A$ ,  $A_{syn}$  and  $A_{data}$  represent the amplitude coefficient, the FRS traces amplitude of the synthetic and the data, respectively. Whereas  $M_B$  is a product of the difference between the width of synthetic ( $W_{syn}$ ) and data ( $W_{data}$ ) and the difference between the maximum FRS trace amplitudes of the synthetic ( $P_{syn}$ ) and the data ( $P_{data}$ ) (revised from Zhao et al., 2017). Only the fit coefficient of the main peak/trough of FRS traces is calculated because it represents ULVZ/HVL structure energy. An example of the fit coefficient calculation is presented in Figure 4.

In the searching process, it is found that the density does have an effect on the amplitude of the  $S^U$  (S pre/postcursors). However, in our density range ( $0\%$ – $10\%$ ), the arrival time and shape of  $S^U$  mainly depend on the thickness and velocity while the density is the second-order factor (Figure S2 in Supporting Information S1). Therefore, the density is not very well constrained.

### 3.3. ULVZ/HVL Characteristics

Our best-fitting models show ULVZ structures with thickness of 11–16 km and S velocity reduction of  $12\%$ – $24\%$  (Figure 5). On the other hand, FRS stacks are best fitted by high-velocity layers (HVL) with thickness ranging from 20–30 km and velocity increase of  $3\%$ – $4\%$  (Figure 5).

There are trade-offs between the thickness and velocity variations in the models (shown in Figure 4). For example, with thickness range from 11 to 16 km, and velocity decrease from  $12\%$  to  $24\%$ , the values of FC are all greater than 0.9 (deep red in Figure 4). In this case, we could not judge one model is definitely better than other ones. Therefore, we constrain our best models in a range.

## 4. D'' Discontinuity Outside the African LLSVP

We also investigate S waves in distance range of  $70^\circ$ – $80^\circ$ , which show clear Scd phases (Figure 6). We remove instrument response of the displacement records, rotate them to great circle path, and band-pass filter them from 0.05 to 1 Hz. Both radial and transverse components are considered. For the data selection, we first calculate SNR of the S waveform, and select those with  $SNR > 5$ ; then we check the data again by eye, to further discard the

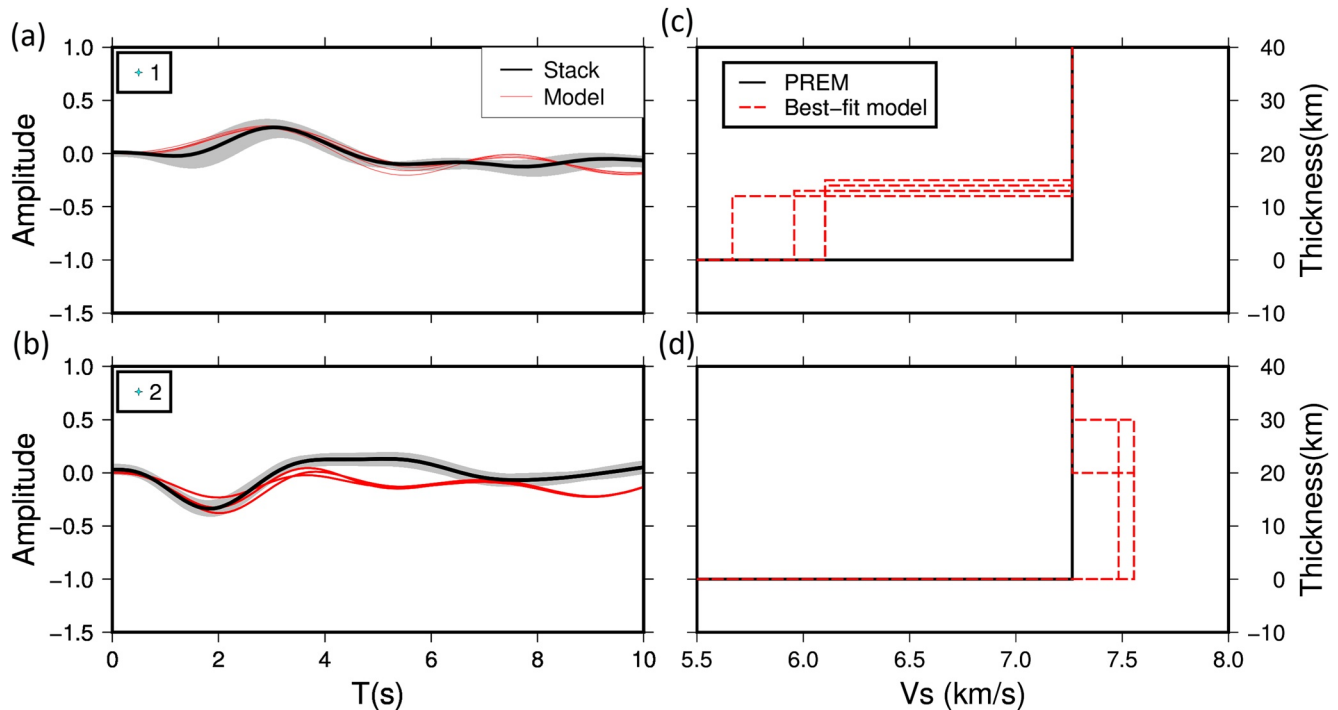


**Figure 5.** Waveform modeling of flip-reverse-stack (FRS) traces in different areas. (Left column) Stacked (black) and synthetic (red)  $S^U$  waveforms in (a) positive peak FRS trace and (b) negative peak. The gray shaded area is the error bound of stacked data. Models used in the synthetics are shown in the right. (Right column) Models used to fit the positive peak observation (c) and negative peak observation (d). The preliminary reference Earth model velocity model (black line) and the best fitting velocity models (dashed red lines) above the core mantle boundary are plotted.

recordings that do not show clear S or ScS. The final data set contains 383 recordings (both radial and transverse components, Figures 6c and 6d).

We utilize AxiSEM (Nissen-Meyer et al., 2014), a parallel spectral-element method, to model the D" discontinuity layer. The reference model is preliminary reference Earth model (PREM, Dziewonski & Anderson, 1981). Various models are tested in order to fit both the SH and SV component of the data. We test different one-dimensional velocity models with variable velocity gradients (Figure S3 in Supporting Information S1), we also test two-dimensional models (Figure S4 in Supporting Information S1), and models with and without low velocity layers above and at the bottom of the D" layer (Figure S5 in Supporting Information S1). Our tests show that two-dimensional models are better to fit data in different azimuths. Moreover, in order to fit the amplitudes and arriving times of Scd at different distance ranges, a low velocity layer on top of D" is needed. A low velocity layer at the bottom of the model is also required, for the purpose of fitting the timing and relative amplitudes of the large distance waveforms (S, Scd and ScS phases in both components, SKS phase in SV components are all considered).

We test different two-dimensional models, which have different thicknesses and velocity variations in the two low velocity layers. We also vary the D" velocity increases as well as the positions of the D" eastern boundary (Figure S4 in Supporting Information S1). Finally we find our best model (Figure 6). It has a 100-km low velocity layer above the D" discontinuity (from 250 to 350 km above the CMB) with shear wave velocity decrease of 3%; Below this layer, the velocity then gradually increases to 2% relative to PREM, and decrease again with 1.5% Vs reduction at the bottom 100 km of the lowermost mantle. Note that the western boundary of the D" layer is not constrained because of the data coverage.

Part of these data have actually been investigated previously (Yao et al., 2015). However, with the low velocity layer at the top of the D" discontinuity, our model fit the data much better in both SH and SV component. For example, on the SH components, a more obvious Scd phase appears at distance greater than 74°, and then it disappears gradually at distances smaller than 74° (Figure 6c). Our model fit this merging waveforms and amplitude

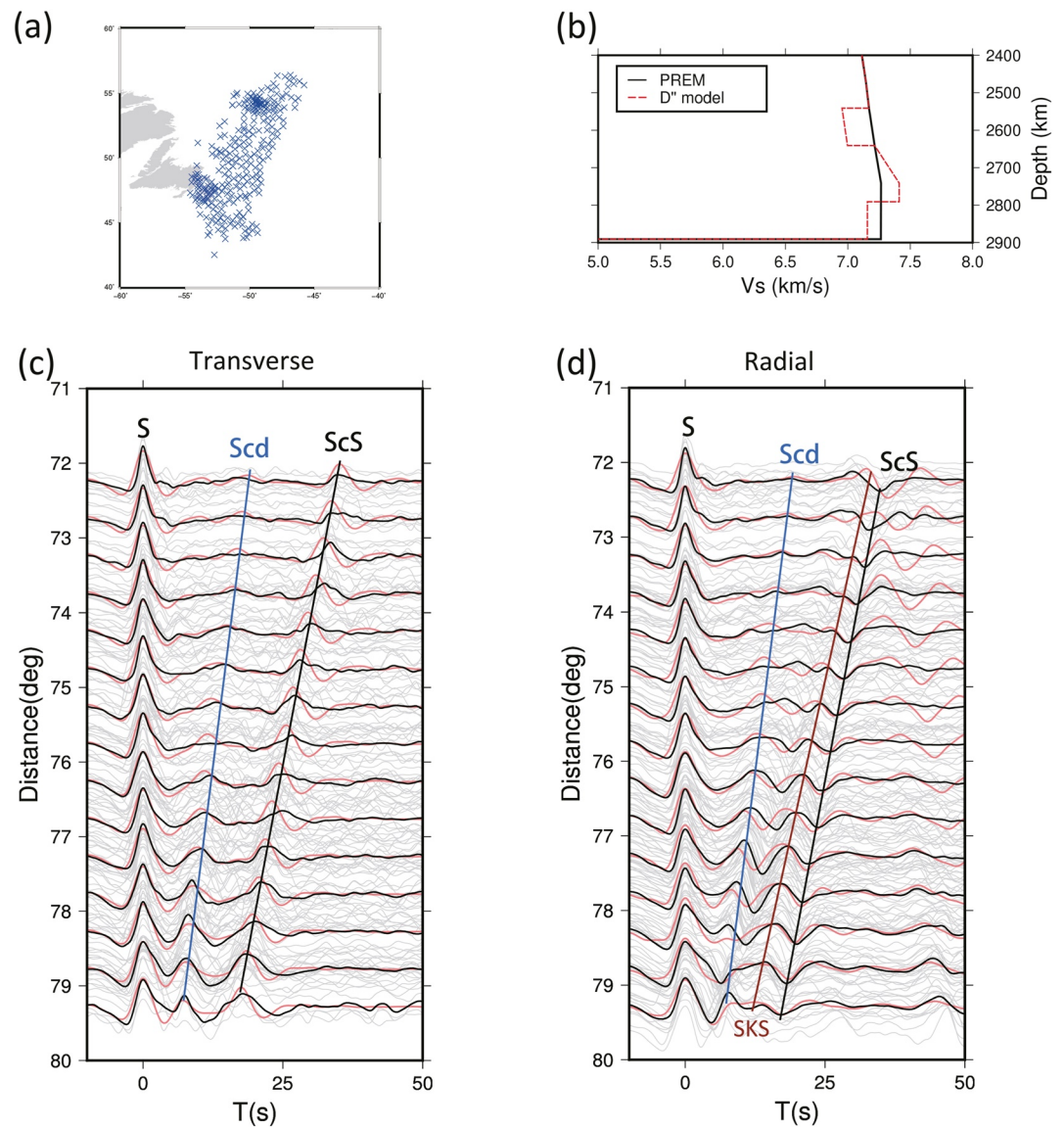


**Figure 6.** Comparison of the synthetic and observed S waveforms from D'' structures. (a) Study area of Scd phases. Blue crosses are ScS bounce points. (b) The best fit S velocity model (red line) near the core mantle boundary (CMB) in our study region. Obvious low velocity layers above the D'' and the CMB are seen in our model. Preliminary reference Earth model (back line) is shown as comparison. (c) and (d) are seismic waveforms in transverse and radial component, respectively. Raw data (gray line) are stacked for every 0.5° (black lines), and synthetic waveforms (red lines) are superposed on them. Note that clear Scd emerge in between S and ScS phases after the epicenter distance of 74°.

of Scd phases much better. Moreover, our model fit the S, Scd, ScS, and SKS phases in radial component as well too (Figures 6c and 6d).

## 5. Discussion and Implications

### 5.1. CMB Structures Across the Northwestern Boundary of the African LLSVP

The velocity profiles at the lowermost mantle across the north Atlantic show complicated structure variations in a distance range of about 20° (Figures 7 and 8). From west in the middle Atlantic to east at the northwest boundary of the African LLSVP, there is clear transition from D'' layer to relatively thin high-velocity layer (HVL) then to ULVZ (ScS rays passing through them are shown in Figure 8). The D'' discontinuity is located in the easternmost

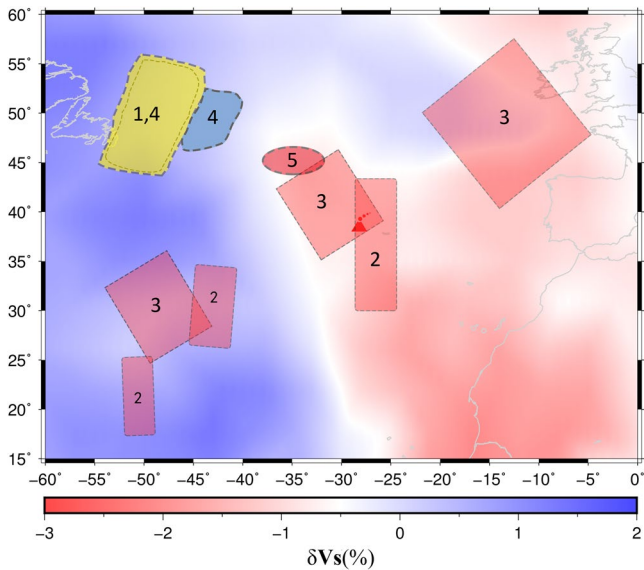


**Figure 7.** Map of Ultra-low Velocity Zones (ULVZ) and D'' locations from various studies. Light and bold dashed outlines represent previous studies and this study, respectively. Yellow patch is D'' discontinuity location what detected by Scd phase (1, Yao et al., 2015; 4, this study); red patches represent ULVZ locations, which are detected by PKKP<sub>ab</sub> (2, Ma & Sun, 2017; 3, Rost & Garnero, 2006) and ScS (5, this study); blue patch is the location of HVL (4, this study). The volcano symbol represents the location of Azores hotspot. Background is S velocity model from GYPsUM (Simmons et al., 2010).

boundary of the paleo Farallon plate (e.g., Bunge & Grand, 2000; Conrad et al., 2004; Simmons et al., 2015). Hence, the D'' discontinuity is very likely related to the remnant of the subducted slab (Goes et al., 2017).

The position of HVL seems to coincide with the boundary of the high and low velocity regions at the CMB in mantle tomography results (e.g., Ritsema et al., 2011; Simmons et al., 2010). Additionally, geodynamic modeling shows that the mantle flow in this region is in the transition from down-welling to up-welling (Conrad et al., 2004). Therefore, the HVL could be from mixing of the ancient slab with the ambient mantle.

ULVZ structures have been found in regions very near to our study area (Ma & Sun, 2017; Rost & Garnero, 2006) (Figure 7). In our study, the best-fit model has and the S wave velocity reduction of 12%–24%, and a thickness of 11–16 km (similar to the inferred minimum thickness of Rost & Garnero, 2006). Ma and Sun (2017) identified ULVZs nearby, which is characterized with 8.5% P wave reductions; at nearby locations further northwest, Rost and Garnero (2006) also found ULVZ structures with an averaged P wave reduction of about 10%. If these ULVZs are of the same origin, the ratio of S wave velocity reduction from our study and P wave velocity reduction from previous study is around 2–3:1, which suggests thermal effect/partial melting may be involved in the ULVZ formation (Berryman, 2000; Williams & Garnero, 1996). Previous studies (e.g., Rost et al., 2005; Yuan & Romanowicz, 2017) show that hot spots may serve as the thermal source and we find that near our study area, which is possible that this hotspot may rise obliquely from the deep mantle near the boundary of the Africa LLSVP. Therefore, the existence of Azores hotspot can provide heat for ULVZ formation. Besides, although ULVZs formed of slab associated material have been hypothesized,

in this scenario it is unlikely to provide a valid explanation for our observations because the locations of slab seem to be a bit far away from the ULVZ, thus we don't consider this scenario.

The Pacific and African LLSVPs share some similarities as well as differences. Recent studies have demonstrated that the Pacific LLSVP have steep edges at the eastern/northeastern (e.g., Deng et al., 2017; Frost & Rost, 2014) and western boundaries (He & Wen, 2009, 2012). On the northeastern boundary of mid-Pacific LLSVP, the locations of the ULVZ and D'' layer as well as the shapes of LLSVP edges are strongly affected by the subducted slab reaching the CMB (Sun et al., 2019), similar to the scenario at the eastern boundary of the African LLSVP (Reiss et al., 2019). In this case, slab push may affect the incline of the LLSVP and the location of the ULVZ. Moreover, considering the locations of these structures, formation of the ULVZ may also be related to the slab materials (e.g., Hu et al., 2016; Liu et al., 2016)

However, in our study region at the northwestern boundary of the African LLSVP, we do not observe direct interactions between the LLSVP/ULVZ and subducted slabs. Instead, we observe HVL in between the D'' discontinuity and ULVZ near the African LLSVP. Such a transition suggests that the slab may mix with ambient mantle in geological time, and weakly affect ULVZ in far field.

## 5.2. Low Velocity Layer on Top of D'' Discontinuity

There is clear low velocity layer on top of the D'' discontinuity in our model. Although this low velocity layer has been reported in previous studies (e.g., He & Wen, 2011; Kawai & Tsuchiya, 2009; Li et al., 2019; Sun et al., 2016; Yao et al., 2015), however, its causes have not yet been fully explored.

One possible cause is thermal effects, in which additional heat release/accumulation may cause softening or partial melting near the D''. We noticed that the transition from bridgmanite to post-perovskite (ppv), which caused the D'' discontinuity, is an exothermic phase change with its Clapeyron slope (Kawai & Tsuchiya, 2009; Murakami et al., 2004; Oganov & Ono, 2004; Tsuchiya et al., 2004); and the thermal diffusivity of post-perovskite is higher than that of bridgmanite (e.g., Hunt et al., 2012; Nakagawa & Tackley, 2004). These may trap additional heat at the top of D'' and cause partial melting or softening of the material. However, based on the



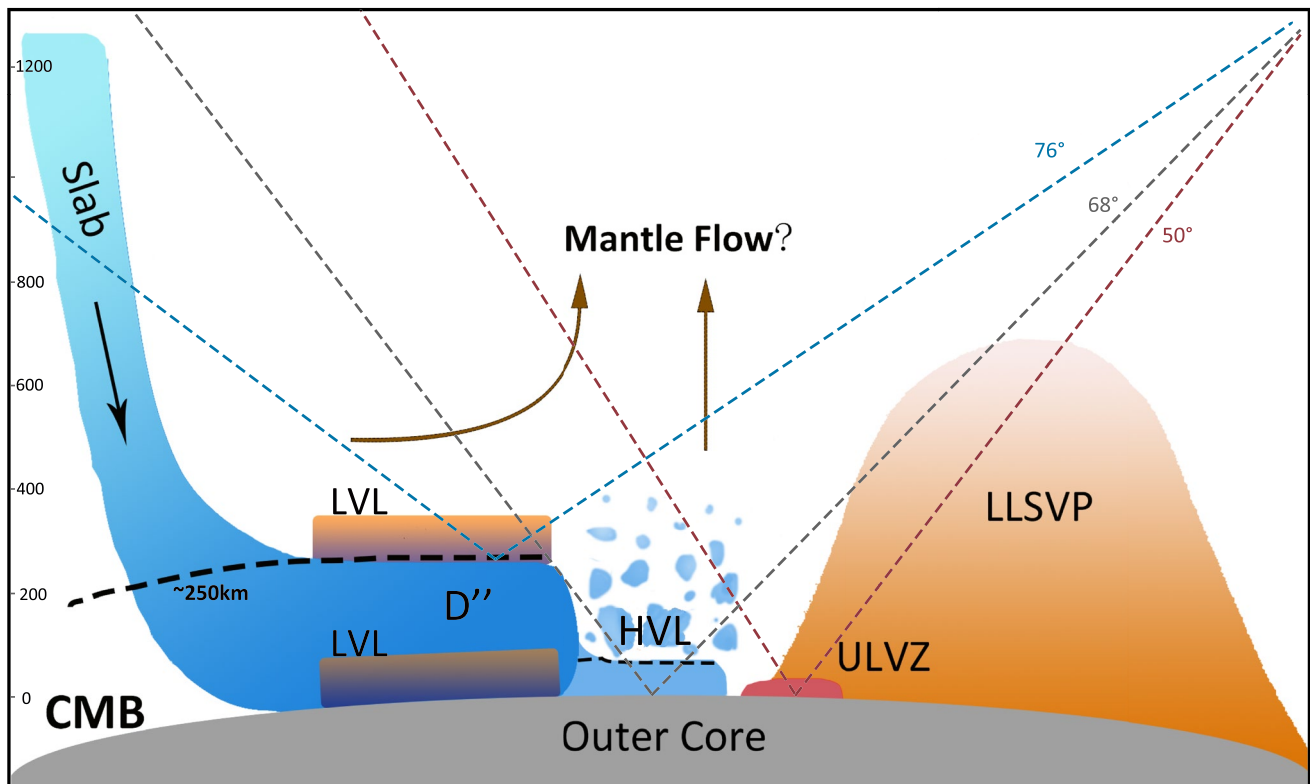


**Figure 8.** Schematic cartoon showing raypath of ScS phase and the lateral structure changes across the north Atlantic to near the northwest boundary of the African Large Low 21 Shear Velocity Zones (LLSVP). The three ScS rays pass through the Ultra-low Velocity Zones (ULVZ (red)), high-velocity layer (HVL, light blue), low-velocity layer (LVL, light brown) and D'' discontinuity (dark blue) at epicenter distances of 50°, 68° and 76° (red, gray and blue dash lines), respectively. The paleo-subduction slab (dark blue blocks) sunk into the lowermost mantle, which formed the D'' discontinuity layer and two LVL. The foremost part of the slab may mix with ambient mantle in the context of mantle flow (brown arrows) and form a thin HVL. Further east near the boundary inside the LLSVP, ULVZ is formed, which may be affected by thermal or other compositional changes.

thermal parameters of bridgmanite and the post perovskite (Wu, 2016), we calculate that 2% velocity reduction needs more than one thousand kelvin temperature change. This scenario is not possible.

Other possibilities for the low velocity could be compositional or phase change related to subducted slab. Studies show that in the lower mantle conditions (e.g., at 3000–4000K, 120Gpa), cubic Ca-perovskite (CaPv) has about 2% Vs reductions and 2.5% density increase than Fe-bearing Mg-Pv (e.g., Kawai & Tsuchiya, 2015). Moreover, its density is lower than that of the post perovskite (ppv) (Murakami et al., 2004). Hence, when the CaPv of subducted oceanic crust accumulate at the top of D'' discontinuity, it provides a possible explanation for the low velocity layer there. Moreover, MORB in the oceanic crust in the lower mantle condition (bottom 200–300 km of the lower mantle) also has a 2.2% velocity reduction compared to PREM (Zhao et al., 2018). Thus, we propose that the S wave velocity reduction at the top of D'' discontinuity is very likely related to the subducted Farallon slab.

If it is true that small-scale upwelling developing at the edge of slabs can cause low velocity layer as well (Li et al., 2019), then it is possible that subducted Farallon slab can interact with upwelling at its edge, thus cause the low velocity we observed.

It is generally believed that the velocity decrease of the bottom of D'' discontinuity layer is related to the reverse phase transition from ppv to bridgmanite (Lay et al., 2006). Kawai and Tsuchiya (2009) suggest that the reverse transition together with increasing temperature would produce a velocity reduction of up to 5%, which is consistent with the reduction of the bottom of D'' discontinuity. Moreover, the average velocity in the lowermost mantle would decrease with the increase of Fe and Al impurity content (Tsuchiya & Tsuchiya, 2006). Therefore, the reverse transition, together with composition variations would be the cause of the low velocity layer at the bottom of the D'' layer.

## 6. Conclusions

In this paper, using various waveforms and techniques, we detect different velocity structures above the core mantle boundary across a long east-west profile from northwest boundary of the African LLSVP to the mid-Atlantic.

An ULVZ is detected near the northwest boundary of the African LLSVP; Our results show that it is 11–16 km in thickness, with a 12%–24% reduction in  $V_s$ . Moreover, a thin high-velocity layer (HVL) and  $D''$  discontinuity are also detected outside the LLSVP in the further to the west of our study region. The thickness of the HVL ranges from 20 to 30 km and shows a  $V_s$  increase of 3%–4%. Even further west  $D''$  discontinuity is observed at ~250 km high above the CMB with a shear velocity increase of 2%. In addition, there is a low velocity layer at top of  $D''$ , whose  $V_s$  reduction is 3% and the thickness is about 100 km, while there is another low velocity layer at the base of  $D''$  with  $V_s$  reduction is of 1.5% and thickness is of 100 km.

The transition of different structures across the northwestern boundary of the African LLSVP suggests interactions of slab and LLSVP material with the ambient mantle, which may modify the thermal state and/or composition above the CMB, and result in different structures. We suggest that thermal effects or the remnants of a basal magma ocean may play important roles in the origin of the ULVZ. We also propose that the low velocity layer we observe above the  $D''$  is very likely related to Ca-Pv from the subducted Farallon slab and upwelling flow, rather than the thermal effect.

The results in this paper provide a good case for understanding large scale structure transition near the CMB region. Further small-scale structure investigations may be needed to unravel the detailed process.

## Data Availability Statement

Seismic data from the USArray and Africa networks are accessed via the IRIS Data Management Center (IRIS: [www.iris.edu](http://www.iris.edu)).

## References

- Avants, M., Lay, T., & Garnero, E. J. (2006). A new probe of ULVZ S-wave velocity structure: Array stacking of ScS waveforms. *Geophysical Research Letters*, *33*, L07314. <https://doi.org/10.1029/2005GL024989>
- Berkhout, A. J. (1977). Least-squares inverse filtering and wavelet deconvolution. *Geophysics*, *42*, 1369–1383. <https://doi.org/10.1190/1.1440798>
- Berryman, J. G. (2000). Seismic velocity decrement ratios for regions of partial melt in the lower mantle. *Geophysical Research Letters*, *27*, 421–424. <https://doi.org/10.1029/1999gl1008402>
- Brown, S. P., Thorne, M. S., Miyagi, L., & Rost, S. (2015). A compositional origin to ultralow-velocity zones. *Geophysical Research Letters*, *42*, 1039–1045. <https://doi.org/10.1002/2014gl062097>
- Buffett, B. A., Garnero, E. J., & Jeanloz, R. (2000). Sediments at the top of Earth's core. *Science*, *290*, 1338–1342. <https://doi.org/10.1126/science.290.5495.1338>
- Bunge, H.-P., & Grand, S. P. (2000). Mesozoic plate-motion history below the northeast Pacific Ocean from seismic images of the subducted Farallon slab. *Nature*, *405*, 337–340. <https://doi.org/10.1038/35012586>
- Christensen, U. R., & Hofmann, A. W. (1994). Segregation of subducted oceanic crust in the convecting mantle. *Journal of Geophysical Research: Solid Earth*, *99*, 19867–19884. <https://doi.org/10.1029/93jb03403>
- Conrad, C., Lithgow-Bertelloni, C., & Louden, K. (2004). Iceland, the Farallon slab, and dynamic topography of the North Atlantic. *Geology*, *32*, 177. <https://doi.org/10.1130/G20137.1>
- Cottaar, S., & Romanowicz, B. (2012). An unusually large ULVZ at the base of the mantle near Hawaii. *Earth and Planetary Science Letters*, *355–356*, 213–222. <https://doi.org/10.1016/j.epsl.2012.09.005>
- Courtier, A. M., Bagley, B., & Revenaugh, J. (2007). Whole mantle discontinuity structure beneath Hawaii. *Geophysical Research Letters*, *34*, L17304. <https://doi.org/10.1029/2007gl031006>
- Cummins, P. R., Takeuchi, N., & Geller, R. J. (1997). Computation of complete synthetic seismograms for laterally heterogeneous models using the Direct Solution Method. *Geophysical Journal International*, *130*, 1–16. <https://doi.org/10.1111/j.1365-246X.1997.tb00983.x>
- Deng, J., Long, M. D., Creasy, N., Wagner, L., Beck, S., Zandt, G., et al. (2017). Lowermost mantle anisotropy near the eastern edge of the Pacific LLSVP: Constraints from SKS–SKKS splitting intensity measurements. *Geophysical Journal International*, *210*, 774–786. <https://doi.org/10.1093/gji/ggx190>
- Dziewonski, A. M., & Anderson, D. L. (1981). Preliminary reference Earth model. *Physics of the Earth and Planetary Interiors*, *25*, 297–356. [https://doi.org/10.1016/0031-9201\(81\)90046-7](https://doi.org/10.1016/0031-9201(81)90046-7)
- Frost, D. A., & Rost, S. (2014). The P-wave boundary of the large-low shear velocity province beneath the Pacific. *Earth and Planetary Science Letters*, *403*, 380–392. <https://doi.org/10.1016/j.epsl.2014.06.046>
- Goes, S., Agrusta, R., van Hunen, J., Garel, F. (2017). Subduction-transition zone interaction: A review. *Geosphere*, *13*(3), 644–664. <https://doi.org/10.1130/GES01476.1>
- He, Y., & Wen, L. (2009). Structural features and shear-velocity structure of the “Pacific Anomaly”. *Journal of Geophysical Research*, *114*, 1–17. <https://doi.org/10.1029/2008JB005814>
- He, Y., & Wen, L. (2012). Geographic boundary of the “Pacific Anomaly” and its geometry and transitional structure in the north. *Journal of Geophysical Research*. (ISSN 0148-0227), *117*(B9), 1–16. <https://doi.org/10.1029/2012JB009436>

## Acknowledgments

This work is supported by the National Science Foundation of China (No. 41774053; No. 42074059) and the Strategic Priority Research Program (B) of the Chinese Academy of Sciences (Grant NO. XDB42020304). Maps in the paper are made by Generic Mapping Tools (Wessel & Smith, 1998). The AxiSEM program is performed on the Milkyway-II super-computer cluster of Super Computation Center in Guangzhou.

- He, Y. M., & Wen, L. X. (2011). Seismic velocity structures and detailed features of the D'' discontinuity near the core-mantle boundary beneath eastern Eurasia. *Physics of The Earth and Planetary Interiors*, 189(3–4), 176–184. <https://doi.org/10.1016/j.pepi.2011.09.002>
- Helmberger, D., Ni, S., Wen, L., & Ritsema, J. (2000). Seismic evidence for ultralow-velocity zones beneath Africa and eastern Atlantic. *Journal of Geophysical Research: Solid Earth*, 105(B10), 23865–23878. <https://doi.org/10.1029/2000JB900143>
- Hu, Q., Kim, D. Y., Yang, W., Yang, L., Meng, Y., Zhang, L., & Mao, H.-K. (2016). FeO<sub>2</sub> and FeOOH under deep lower-mantle conditions and Earth's oxygen–hydrogen cycles. *Nature*, 534, 241–244. <https://doi.org/10.1038/nature18018>
- Hunt, S. A., Davies, D. R., Walker, A. M., McCormack, R. J., Wills, A. S., Dobson, D. P., & Li, L. (2012). On the increase in thermal diffusivity caused by the perovskite to post-perovskite phase transition and its implications for mantle dynamics. *Earth and Planetary Science Letters*, 319, 96–103. <https://doi.org/10.1016/j.epsl.2011.12.009>
- Kawai, K., Takeuchi, N., & Geller, R. J. (2006). Complete synthetic seismograms up to 2 Hz for transversely isotropic spherically symmetric media. *Geophysical Journal International*, 164, 411–424. <https://doi.org/10.1111/j.1365-246X.2005.02829.x>
- Kawai, K., & Tsuchiya, T. (2009). Temperature profile in the lowermost mantle from seismological and mineral physics joint modeling. *Proceedings of the National Academy of Sciences*, 106(52), 22119–22123. <https://doi.org/10.1073/pnas.0905920106>
- Kawai, K., & Tsuchiya, T. (2015). Small shear modulus of cubic CaSiO<sub>3</sub> perovskite. *Geophysical Research Letters*, 42, 2718–2726. <https://doi.org/10.1002/2015GL063446>
- Labrosse, S., Hernlund, J. W., & Coltice, N. (2007). A crystallizing dense magma ocean at the base of the Earth's mantle. *Nature*, 450, 866–869. <https://doi.org/10.1038/nature06355>
- Lay, T., Hernlund, J., Garnero, E. J., & Thorne, M. S. (2006). A post-perovskite lens and D'' heat flux beneath the central Pacific. *Science*, Nov 24, 314(5803), 1272–1276. <https://doi.org/10.1126/science.1133280>
- Levinson, N. (1946). The Wiener (root mean square) error criterion in filter design and prediction. *Journal of Mathematics and Physics*, 25(1–4), 261–278. <https://doi.org/10.1002/sapm1946251261>
- Li, Y., Miller, M. S., & Sun, D. (2019). Seismic imaging the D'' region beneath the Central Atlantic. *Physics of the Earth and Planetary Interiors*, 292, 76–86. <https://doi.org/10.1016/j.pepi.2019.05.005>
- Liu, J., Li, J., Hrubciak, R., & Smith, J. S. (2016). Origins of ultralow velocity zones through slab-derived metallic melt. *Proceedings of the National Academy of Sciences*, 113, 5547–5551. <https://doi.org/10.1073/pnas.1519540113>
- Ma, X., & Sun, X. (2017). Ultra-low velocity zone heterogeneities at the core–mantle boundary from diffracted PKKPab waves. *Earth Planets and Space*, 69, 115. <https://doi.org/10.1186/s40623-017-0692-5>
- Ma, X., Sun, X., & Thomas, C. (2019). Localized ultra-low velocity zones at the eastern boundary of Pacific LLSVP. *Earth and Planetary Science Letters*, 507, 40–49. <https://doi.org/10.1016/j.epsl.2018.11.037>
- Mao, W. L., Mao, H.-k., Sturhahn, W., Zhao, J., Prakapenka, V. B., Meng, Y., et al. (2006). Iron-Rich post-perovskite and the origin of ultralow-velocity zones. *Science*, 312, 564–565. <https://doi.org/10.1126/science.1123442>
- Masters, G., Laske, G., Bolton, H., & Dziewonski, A. M. (2000). The relative behavior of shear velocity, bulk sound speed, and compressional velocity in the mantle: Implications for chemical and thermal structure. In *Earth's deep interior: Mineral physics and tomography from the atomic to the global scale*, *Geophysical Monograph Series* (pp. 63–87). American Geophysical Union. <https://doi.org/10.1029/GM117p0063>
- Montelli, R., Nolet, G., Dahlen, F. A., Masters, G., Engdahl, E. R., & Hung, S. H. (2004). Finite-frequency tomography reveals a variety of plumes in the mantle. *Science*, 303, 338–343. <https://doi.org/10.1126/science.1092485>
- Murakami, M., Hirose, K., Kawamura, K., Sata, N., & Ohishi, Y. (2004). Post-perovskite phase transition in MgSiO<sub>3</sub>. *Science*, 304, 855–858. <https://doi.org/10.1126/science.1095932>
- Nakagawa, T., & Tackley, P. J. (2004). Effects of a perovskite-post perovskite phase change near core-mantle boundary in compressible mantle convection. *Geophysical Research Letters*, 31, L16611. <https://doi.org/10.1029/2004GL020648>
- Ni, S., & Helmberger, D. V. (2003). Seismological constraints on the South African superplume: could be the oldest distinct structure on earth. *Earth and Planetary Science Letters*, 206, 119–131. [https://doi.org/10.1016/s0012-821x\(02\)01072-5](https://doi.org/10.1016/s0012-821x(02)01072-5)
- Ni, S., Tan, E., Gurnis, M., & Helmberger, D. (2002). Sharp sides to the African superplume. *Science*. (ISSN 1095-9203), 296, 1850–1852. <https://doi.org/10.1126/science.1070698>
- Nissen-Meyer, T., van Driel, M., Stähler, S. C., Hosseini, K., Hempel, S., Auer, L., et al. (2014). AxiSEM: Broadband 3-D seismic wavefields in axisymmetric media. *Solid Earth*, 5, 425–445. <https://doi.org/10.5194/se-5-425-2014>
- Nomura, R., Ozawa, H., Tateno, S., Hirose, K., Hernlund, J., Muto, S., et al. (2011). Spin crossover and iron-rich silicate melt in the Earth's deep mantle. *Nature*, 473, 199–202. <https://doi.org/10.1038/nature09940>
- Oganov, A. R., & Ono, S. (2004). Theoretical and experimental evidence for a post-perovskite phase of MgSiO<sub>3</sub> in Earth's D'' layer. *Nature*, 430, 445–448. <https://doi.org/10.1038/nature02701>
- Rawlinson, N., & Kennett, B. L. N. (2004). Rapid estimation of relative and absolute delay times across a network by adaptive stacking. *Geophysical Journal International*, 157, 332–340. <https://doi.org/10.1111/j.1365-246X.2004.02188.x>
- Reiss, M. C., Long, M. D., & Creasy, N. (2019). Lowermost mantle anisotropy beneath Africa from differential SKS-SKKS shear-wave splitting. *Journal of Geophysical Research: Solid Earth*, 124, 8540–8564. <https://doi.org/10.1029/2018jb017160>
- Ritsema, J., Deuss, A., van Heijst, H. J., & Woodhouse, J. H. (2011). S40RTS: A degree-40 shear-velocity model for the mantle from new Rayleigh wave dispersion, teleseismic traveltime and normal-mode splitting function measurements. *Geophysical Journal International*, 184, 1223–1236. <https://doi.org/10.1111/j.1365-246X.2010.04884.x>
- Ritsema, J., Lay, T., Garnero, E. J., & Benz, H. (1998). Seismic anisotropy in the lowermost mantle beneath the Pacific. *Geophysical Research Letters*, 25(8), 1229–1232. <https://doi.org/10.1029/98gl00913>
- Rondenay, S., & Fischer, K. M. (2003). Constraints on localized core-mantle boundary structure from multichannel, broadband SKS coda analysis. *Journal of Geophysical Research*, 108(B11), 2337. <https://doi.org/10.1029/2003jb002518>
- Rost, S., Garnero, E., Williams, Q., & Manga, M. (2005). Seismological constraints on a possible plume root at the core–mantle boundary. *Nature*, 435, 666–669. <https://doi.org/10.1038/nature03620>
- Rost, S., & Garnero, E. J. (2006). Detection of an ultralow velocity zone at the core-mantle boundary using diffracted PKKPab waves. *Journal of Geophysical Research*, 111, B07309. <https://doi.org/10.1029/2005jb003850>
- Rost, S., Garnero, E. J., & Williams, Q. (2006). Fine-scale ultralow-velocity zone structure from high-frequency seismic array data. *Journal of Geophysical Research*, 111(B9), B09310. <https://doi.org/10.1029/2005jb004088>
- Simmons, N. A., Forte, A. M., Boschi, L., & Grand, S. P. (2010). GyPSuM: A joint tomographic model of mantle density and seismic wave speeds. *Journal of Geophysical Research*, 115, B12310. <https://doi.org/10.1029/2010jb007631>
- Simmons, N. A., & Grand, S. P. (2002). Partial melting in the deepest mantle. *Geophysical Research Letters*, 29, 47–41–47–44. <https://doi.org/10.1029/2001gl013716>

- Simmons, N. A., Myers, S. C., & Johannesson, G. (2011). Global-scale P wave tomography optimized for prediction of teleseismic and regional travel times for Middle East events: 2. Tomographic inversion. *Journal of Geophysical Research*, *116*(B4), B04305. <https://doi.org/10.1029/2010jb007969>
- Simmons, N. A., Myers, S. C., Johannesson, G., Matzel, E., & Grand, S. P. (2015). Evidence for long-lived subduction of an ancient tectonic plate beneath the southern Indian Ocean. *Geophysical Research Letters*, *42*, 9270–9278. <https://doi.org/10.1002/2015GL066237>
- Sun, D., Helmberger, D., Jackson, J. M., Clayton, R. W., & Bower, D. J. (2013). Rolling hills on the core-mantle boundary. *Earth and Planetary Science Letters*, *361*, 333–342. <https://doi.org/10.1016/j.epsl.2012.10.027>
- Sun, D., Helmberger, D., Lai, V. H., Gurnis, M., Jackson, J. M., & Yang, H.-Y. (2019). Slab control on the Northeastern edge of the mid-Pacific LLSVP near Hawaii. *Geophysical Research Letters*, *46*, 3142–3152. <https://doi.org/10.1029/2018gl081130>
- Sun, D., Helmberger, D., Miller, M. S., & Jackson, J. M. (2016). Major disruption of D" beneath Alaska. *Journal of Geophysical Research: Solid Earth*, *121*, 3534–3556. <https://doi.org/10.1002/2015jb012534>
- Sun, D., & Miller, M. S. (2013). Study of the western edge of the African large low shear velocity province. *Geochemistry, Geophysics, Geosystems*, *14*(8), 3109–3125. <https://doi.org/10.1002/ggge.20185>
- Sun, D., Song, T. R. A., & Helmberger, D. (2006). Complexity of D" in the presence of slab-debris and phase changes. *Geophysical Research Letters*, *33*, L12S07. <https://doi.org/10.1029/2005GL025384>
- Sun, N., Wei, W., Han, S., Song, J., Li, X., Duan, Y., et al. (2018). Phase transition and thermal equation of state of (Fe,Al)-bridgmanite and post-perovskite: Implication for the chemical heterogeneity at the lowermost mantle. *Earth and Planetary Science Letters*, *490*, 161–169. <https://doi.org/10.1016/j.epsl.2018.03.004>
- Tao, J., Hu, J., Jin, C., & He, X. (2020). Seismic evidence links the subducted Mongol-Okhotsk slab to deformation in D" near the northeastern margin of the Perm Anomaly. *Tectonophysics*, *774*, 228297. <https://doi.org/10.1016/j.tecto.2019.228297>
- Thorne, M. S., & Garnero, E. J. (2004). Inferences on ultralow-velocity zone structure from a global analysis of SPdKS waves. *Journal of Geophysical Research*, *109*, B08301. <https://doi.org/10.1029/2004JB003010>
- Thorne, M. S., Garnero, E. J., Jahnke, G., Igel, H., & McNamara, A. K. (2013). Mega ultra low velocity zone and mantle flow. *Earth and Planetary Science Letters*, *364*, 59–67. <https://doi.org/10.1016/j.epsl.2012.12.034>
- Tsuchiya, T., & Tsuchiya, J. (2006). Effect of impurity on the elasticity of perovskite and postperovskite: Velocity contrast across the postperovskite transition in (Mg,Fe,Al)(Si,Al)O<sub>3</sub>. *Geophysical Research Letters*, *33*, L12S04. <https://doi.org/10.1029/2006gl025706>
- Tsuchiya, T., Tsuchiya, J., Umamoto, K., & Wentzcovitch, R. M. (2004). Phase transition in MgSiO<sub>3</sub> perovskite in the earth's lower mantle. *Earth and Planetary Science Letters*, *224*, 241–248. <https://doi.org/10.1016/j.epsl.2004.05.017>
- Vanacore, E. A., Rost, S., & Thorne, M. S. (2016). Ultralow-velocity zone geometries resolved by multidimensional waveform modelling. *Geophysical Journal International*, *206*, 659–674. <https://doi.org/10.1093/gji/ggw114>
- Wang, Y., & Wen, L. (2007). Geometry and P and S velocity structure of the "African Anomaly". *Journal of Geophysical Research*, *112*(B5), B05313. <https://doi.org/10.1029/2006jb004483>
- Wessel, P., & Smith, W. H. F. (1998). New, improved version of the generic mapping Tools released. *Eos Transactions American Geophysical Union*, *79*, 579. <https://doi.org/10.1029/98EO00426>
- Wicks, J. K., Jackson, J. M., & Sturhahn, W. (2010). Very low sound velocities in iron-rich (Mg,Fe)O: Implications for the core-mantle boundary region. *Geophysical Research Letters*, *37*, L15304. <https://doi.org/10.1029/2010gl043689>
- Williams, Q., & Garnero, E. J. (1996). Seismic evidence for partial melt at the base of Earth's mantle. *Science*, *273*, 1528–1530. <https://doi.org/10.1126/science.273.5281.1528>
- Wu, Z. (2016). Velocity structure and composition of the lower mantle with spin crossover in ferropericlae. *Journal of Geophysical Research: Solid Earth*, *121*, 2304–2314. <https://doi.org/10.1002/2015JB012667>
- Wyssession, M. E., Lay, T., Revenaugh, J., Williams, Q., Garnero, E., Jeanloz, R., & Kellogg, L. H. (1998). The D" discontinuity and its implications. In *The core-mantle boundary region. Geodynamic Series* (Vol. 28, pp. 273–297). AGU. <https://doi.org/10.1029/gd028p0273>
- Yao, J., & Wen, L. (2014). Seismic structure and ultra-low velocity zones at the base of the Earth's mantle beneath Southeast Asia. *Physics of the Earth and Planetary Interiors*, *233*, 103–111. <https://doi.org/10.1016/j.pepi.2014.05.009>
- Yao, Y., Whittaker, S., & Thorne, M. S. (2015). D" discontinuity structure beneath the North Atlantic from Scd observations. *Geophysical Research Letters*, *42*, 3793–3801. <https://doi.org/10.1002/2015GL063989>
- Yu, S., & Garnero, E. J. (2018). Ultralow velocity zone locations: A global assessment. *Geochemistry, Geophysics, Geosystems*, *19*, 396–414. <https://doi.org/10.1002/2017gc007281>
- Yuan, K., & Romanowicz, B. (2017). Seismic evidence for partial melting at the root of major hot spot plumes. *Science*, *357*, 393–397. <https://doi.org/10.1126/science.aan0760>
- Zhao, C., Garnero, E. J., Li, M., McNamara, A., & Yu, S. (2017). Intermittent and lateral varying ULVZ structure at the northeastern margin of the Pacific LLSVP. *Journal of Geophysical Research: Solid Earth*, *122*, 1198–1220. <https://doi.org/10.1002/2016JB013449>
- Zhao, M., Zhou, H., Yin, K., Sun, Y., Liu, X., Xu, S., & Lu, X. (2018). Thermoelastic properties of aluminous phases in MORB from first-principle calculation: Implications for Earth's lower mantle. *Journal of Geophysical Research: Solid Earth*, *123*, 10583–10596. <https://doi.org/10.1029/2018JB016491>